


Article

Highly Active, High Specific Surface Area Fe/C/N ORR Electrocatalyst from Liquid Precursors by Combination of CO₂ Laser Pyrolysis and Single NH₃ Thermal Post-Treatment

Henri Perez ^{1,*}, Virginie Jorda ¹, Jackie Vigneron ², Mathieu Frégnaux ² , Arnaud Etcheberry ², Axelle Quinsac ¹, Yann Leconte ¹ and Olivier Sublemontier ¹

¹ CEA, IRAMIS, UMR NIMBE 3685, F-91191 Gif Sur Yvette, France; virginie.jorda@cea.fr (V.J.); axelle.quinsac@cea.fr (A.Q.); yann.leconte@cea.fr (Y.L.); olivier.sublemontier@cea.fr (O.S.)

² UVSQ, CNRS, UMR 8180, ILV, F-78035 Versailles, France; jackie.vigneron@uvsq.fr (J.V.); mathieu.fregnaux@uvsq.fr (M.F.); arnaud.etcheberry@uvsq.fr (A.E.)

* Correspondence: henri.perez@cea.fr; Tel.: +33-1-01-69-08-41-83

Received: 19 March 2019; Accepted: 30 April 2019; Published: 14 May 2019



Abstract: This paper reports original results on the synthesis and characterization of Fe/C/N ORR electrocatalysts obtained by a combination of CO₂ laser pyrolysis and thermal post-treatment. The precursor liquid media, consisting in a 14 g·L⁻¹ iron III acetylacetonate solution in toluene, was aerosolized and then exposed to a CO₂ laser beam for pyrolysis in continuous flow. Ammonia was used in the pyrolysis process, both as the laser wavelength absorbing gas (i.e., energy transfer agent) and as the sole source of nitrogen. After the laser pyrolysis step, the material was submitted to thermal post-treatment under argon on the one hand, and ammonia on another hand. The three materials—one as-prepared, one thermally treated under argon, and one thermally treated under ammonia—were characterized, in particular, through specific surface area determination, XPS analysis, and ORR measurement. It was found that both kinds of thermal treatment significantly improved the ORR performances, which were evaluated on porous electrodes. Indeed, while the as-prepared material showed an ORR onset potential at ≈790 mV vs. the standard hydrogen electrode (SHE) in HClO₄ 1M, the argon treatment increased the latter to ≈820 mV, and the ammonia treatment led to a very high value of ≈910 mV. Selectivities of 3.65 and 3.93 were measured for the argon and ammonia treated materials, respectively. The outstanding ORR performance resulting from the ammonia treatment is probably related to the very high BET specific surface area measured at 1130 m²·g⁻¹, which was notably obtained without using any templating or sacrificial component in the precursor media.

Keywords: laser pyrolysis; non-noble metal electrocatalyst; oxygen reduction

1. Introduction

One of the key points to the widespread development of fuel cell technology is related to the replacement of the platinum-based electrocatalysts widely employed at the cathode of these devices to reduce oxygen. In an acidic media, the so-called Fe/C/N non-noble catalysts are very promising, especially those developing a high specific surface area. Indeed, most of the performing materials recently developed exhibit specific surface areas in the range of 500 to 1100 m²·g⁻¹. They are synthesized from precursors containing carbon, nitrogen, and iron, the latter being known for promoting graphitization and the formation of actives sites towards the Oxygen Reduction Reaction (ORR). The synthesis processes that provide highly performing ORR catalysts involve a sacrificial or a template material component, and/or a multistep procedure that promotes the formation of a high

specific surface area [1]. For example, $1096 \text{ m}^2 \cdot \text{g}^{-1}$ specific surface area materials were obtained from a mixture of polyacrylonitrile and iron chloride in Tetrahydrofuran [2]. A solid was recovered from this mixture, and was subsequently pyrolysed at $600 \text{ }^\circ\text{C}$, before being ball-milled. The final highly active electrocatalyst was obtained after two additional thermal treatments, first at $800 \text{ }^\circ\text{C}$ and then at $1000 \text{ }^\circ\text{C}$, under NH_3 . A sacrificial metal organic framework with a high specific surface area has been also used to obtain highly active materials, also involving a multistep procedure, namely: by mixing with an organic nitrogen containing molecule and an iron salt, drying, ball-milling, and finally, two thermal treatments under argon and then NH_3 . [3,4]. Silica templated syntheses [5] or carbide-derived carbons are also examples providing high-surface area electrocatalysts through multistep processes [6].

Recently, we reported, for the first time, the synthesis of Fe/C/N-type non-noble ORR electrocatalysts using CO_2 laser pyrolysis and ammonia as energy transfer agent [7]. In this latter work, the catalysts were characterized as prepared, after the single-step CO_2 laser pyrolysis process. The liquid precursor media consisted in pyridine, in which an iron source was added. We showed that the ORR performances of the as-prepared materials were related to the so-called R-parameter, defined by the NH_3 flow over the sum of NH_3 flow and Ar flow, the latter Ar flow being used to drive the aerosol to the CO_2 laser beam interaction region. In the present paper, we used the same approach with a different liquid precursor media, in which no nitrogen was present, simply consisting in iron acetylacetonate $\text{Fe}(\text{acac})_3$ dissolved in toluene. Therefore, the only nitrogen source consisted in the ammonia being used as energy transfer agent. Toluene was chosen in order to try to improve the chemical yield of the reaction, which was previously found to decrease dramatically for high R-values. A significant improvement of the chemical yield was expected in order to obtain the required amount of materials for the study of the $1100 \text{ }^\circ\text{C}$ thermal treatments performed under argon on the one hand, and under NH_3 on the other hand, aiming for the improvement of the ORR performance. Indeed, high temperature thermal treatments under argon and/or ammonia are extensively used in synthetic procedures, leading to the formation of Fe/C/N type electrocatalysts. Several decades ago, pyrolysis was found to improve the stability and performances of N-chelates towards the ORR [8]. The different synthetic methods that use different types of precursors containing iron, carbon, and nitrogen, and lead to the highly performing Fe/C/N electrocatalysts, still use one or several thermal treatments [9]. However, as for the early work mentioned above, it is worth noting that the transition by which the precursors are transformed into a carbon-based material with active sites towards the ORR is still not clearly understood. This holds for argon or NH_3 treatments, although both gases induce some different effects, which will be pointed along the paper. In particular, ammonia has a chemical effect that may impact potentially and by different ways, both the specific surface areas of the final electrocatalysts and its nitrogen content.

The pristine, argon treated, and ammonia treated materials were characterized by specific surface area determination, to some extent by X-ray diffraction and electron microscopy, and by X-Ray Photoelectron Spectroscopy (XPS) analysis. The paper considers, successively, the features of the thermally treated materials, the ORR performances in acidic media evaluated on porous electrodes by cyclic voltammetry in HClO_4 1M, and the evaluation of the selectivity of the ORR.

2. Materials and Methods

2.1. Synthesis

Iron III acetylacetonate ($\text{Fe}(\text{C}_5\text{H}_7\text{O}_2)_3$), referred to as $\text{Fe}(\text{acac})_3$, was obtained from Aldrich (St.Louis, MO, USA), and used as received. Toluene was obtained from Merck (Darmstadt, Germany). The liquid precursor media consisted in $\text{Fe}(\text{acac})_3$ dissolved in toluene, at a concentration of $14 \text{ g} \cdot \text{L}^{-1}$. The CO_2 laser pyrolysis was conducted, as described in detail in a previous report, using the same experimental set-up [7]. Briefly, a liquid droplet aerosol was formed using a pyrosol®7901-type piezoelectric aerosol generator from RBI (Meylan, France). The latter was driven using an argon continuous flow, mixed with an ammonia flow just before crossing the CO_2 laser beam. The flows of argon and ammonia

defined the so-called R-parameter (volume flow fraction of ammonia in total gas flow argon + NH₃) set to 0.40, which corresponds to 800 sccm and 1185 sccm NH₃ and argon volume flows, respectively. The material was collected and washed with acetone, using a Soxhlet extractor.

2.2. Characterization

The X-ray diffraction analysis was performed using a Cu K α wavelength. The iron content was measured by X-ray fluorescence, using a previously described procedure [7–10] involving the collection of porous electrodes of a known iron content, prepared on carbon felts Freudenberg H2415 I2C3 (Weinheim, Germany). The specific surface areas were measured using a Micromeritics FlowSorb II 2300 instrument (Micromeritics, GA, USA), by single point Brunauer, Emmett, Teller (BET) measurements, with a gas mixture of 30 vol% N₂ in He. Before measurement, the sample was degassed at 250 °C for 2 h.

2.3. Thermal Treatments

Thermal treatments were performed in a crucible that was positioned in a quartz tube placed in a tubular oven. The amount of as-formed material introduced in the crucible was about 100 mg. For the ammonia treatment, the sample was first swept with pure ammonia for 20 min, then, the oven was heated up to 1100 °C at a speed rate of 50 °C per minute, and this temperature was maintained for 20 min. The heating was then turned off and rapid cooling was ensured by blowing cold air into the tubular oven. After 20 min of argon sweeping at an ambient temperature, the thermally treated powder was collected and weighted. The thermal treatment under argon was performed with the same procedure as for the ammonia treatment.

2.4. XPS Analysis

The surface analysis was performed with a Thermo Electron K-Alpha spectrometer (Thermo Electron, Waltham, MA, USA). The X-ray excitation was the K-alpha aluminum line at 1486.7 eV. A constant analyzer energy (CAE) mode was used for the electron detection (20 eV pass energy value was chosen). The detection of the photoelectrons was perpendicular to the sample surface, which consisted of porous electrodes formed by filtration on the carbon felts provided, with a 30 nm gold layer deposited by vacuum evaporation, before the formation of the nanomaterial layer by filtration. Before XPS analysis, the electrode was submitted to an electrochemical conditioning step, described below.

2.5. Electrochemical Measurement

The cyclic voltammetry (CV) was recorded using a Bio-Logic VMP3 potentiostat (Bio-Logic, Seyssinet-Parizet, France). As described in great detail in several previous papers [7,10,11], the electrochemical measurements were performed on porous electrodes prepared on carbon felts (Freudenberg) by a vacuum-assisted filtration of powder liquid dispersion. Before the ORR CV recording, the porous electrodes were submitted to a conditioning step, aiming at electrolyte impregnation in the electrode porosity. Briefly, it consists in the electrode immersion for 3 to 5 min each time, and successively, in pure ethanol, then, in a 50/50% volume mixture of water and ethanol, and then in pure water. Then, the electrode is immersed in the oxygen saturated electrolyte for ten to fifteen minutes, in order to replace the air that could be still locally entrapped in the electrode porosity, in spite of the wetting steps described above, by pure O₂. After that, the electrode is scanned upon O₂ bubbling at 100 mV/s from 1 V to 40 mV vs. SHE, until a stable voltammogram is obtained. The number of scans involved is between 100 and 200 scans, and generally, the O₂ bubbling is removed for the last 50 cycles, leaving only an O₂ gas blanket above the electrolyte. First, the cycling step allows for a complete consumption of the residual O₂ gas entrapped in the electrode porosity, and second, the dissolution of the iron-based particles, which are accessible to the electrolyte, as reported before in detail, on nitrogen doped carbon nanotubes (N-CNTs) based porous electrodes [10]. After the above reminded conditioning step, the porous electrode was allowed to stand for at least 20 min

in the electrolyte, so as to ensure a reloading of oxygen saturated bulk electrolyte into the electrode porosity. The electrode is then polarized at 1 V vs. ENH for 2 min, and the ORR CV is recorded at $5 \text{ mV}\cdot\text{s}^{-1}$. The same measurement is performed for the argon, allowing for the background corrected ORR CV to be obtained by subtraction. The potentials were measured using a Sodium-Saturated Calomel Electrode (SSCE radiometer analytical). On the CVs shown in the paper, the potentials are reported vs. the standard hydrogen electrode (SHE; $-0.236 \text{ V vs. SSCE}$). The ORR onset potential is determined by the higher potential at which an ORR current is measured on the background-corrected cyclic voltammetry.

The selectivity of the ORR was investigated on porous electrodes, using an original approach initially reported in detail elsewhere [12]. The method has since been exploited in several reports by us [10,11]. Briefly, it consists in an accurate assaying of the hydrogen peroxide, possibly formed during the ORR. The latter is recorded during a chronoamperometric experiment performed under magnetic stirring, at a potential at which the oxygen reduction peak current occurs on the CV recorded at 5 mV/s . This choice is motivated by the fact that the ORR current is then at a maximum. As reported in previous papers [10,11], the peak potential where the ORR peak current appears actually depends on the catalyst loading, until a critical loading is reached. Beyond this critical loading, the peak potential becomes stable, and the selectivity measured is constant. At a given time, a sample of the electrolyte is collected, in which the H_2O_2 is assayed [12]. If detected, the amount of H_2O_2 produced is compared to the charge involved in the ORR at the same given time, which allows for the selectivity to be calculated.

3. Results

3.1. Synthesis and Characterization of the as Formed and Annealed Materials

The synthesis of the material was conducted in the CO_2 laser pyrolysis reactor, schematized in Figure 1.

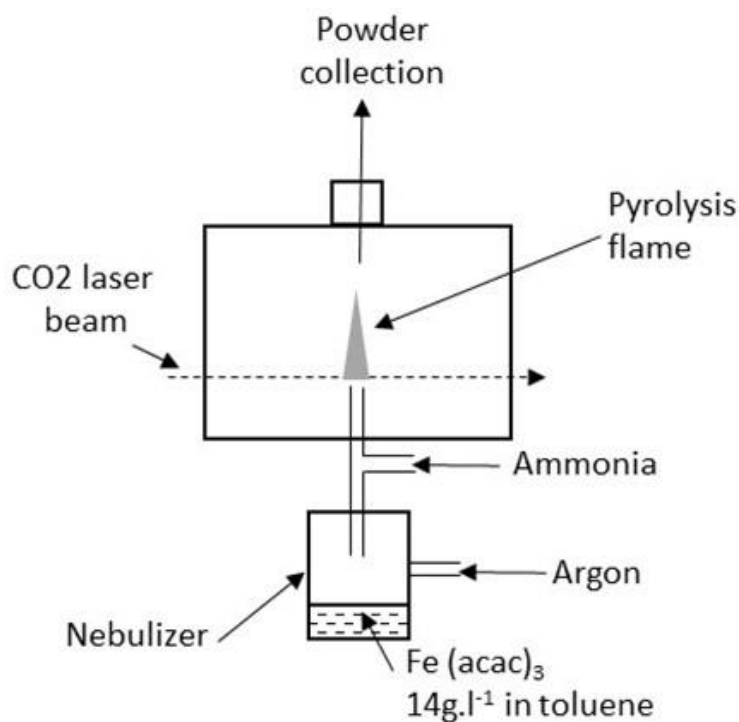


Figure 1. Scheme of the experimental set-up for CO_2 laser pyrolysis.

The material was collected on porous filtering barriers and then washed with acetone to remove the side products of the synthesis, presumably consisting of polycyclic aromatic hydrocarbons. Table 1 reports the production rate and the chemical yield for the synthesis before and after acetone washing.

The chemical yield is defined by the weight ratio of the obtained material over the consumed liquid precursor. Table 1 also reports the specific surface area and the iron content of the material.

Table 1. Feature of the as-prepared material.

Rate Production g·h ⁻¹	Chemical Yield as-Formed wt %	Chemical Yield after Acetone Washing wt %	Specific Surface Area m ² ·g ⁻¹	Iron Content wt %
3.4	12.5	9.5	147	0.9

Although $R = 0.40$ was not investigated in our previous paper [7], a comparison of the data from Table 1 with that previously reported, where R varied in the 0.04–0.67 range, can be considered. As a result, it is seen that the use of toluene instead of pyridine results in a much higher production rate, and strongly improves the chemical yield. Indeed, the pyridine and $\text{Fe}(\text{acac})_3$ precursor gave a $\approx 0.4\%$ chemical yield for R -values higher than 0.36. On the specific surface area side, the values recorded here do not allow for a particular effect of the use of toluene to be established when compared to pyridine. Indeed, for the latter, a clear drop of the specific surface area to $\approx 60 \text{ m}^2\cdot\text{g}^{-1}$ was obtained for $R = 0.60$, while a value of $\approx 150 \text{ m}^2\cdot\text{g}^{-1}$ was obtained for $R = 0.30$. In contrast, the iron content recorded in the present paper is clearly much lower than those recorded with pyridine (10 wt.% for $R = 0.36$ and 20 wt.% for $R = 0.60$). The low iron content obtained here could be related to a more efficient decomposition of toluene, and its better ability to produce carbon-based solids when compared to pyridine.

Two samples of about 100 mg were used to perform annealing at 1100 °C for 20 min under argon or ammonia. Table 2 reports the weight loss recorded after these treatments, and the specific surface areas of the annealed materials.

Table 2. Comparison of the weight loss and specific surface area of the annealed materials under argon and ammonia.

Annealing Conditions	wt % Loss	Specific Surface Area m ² ·g ⁻¹
Annealing under Ar	8.0	153
Annealing under NH ₃	80.2	1130

Treatment under argon induced limited weight loss and an insignificant increase of the specific surface area. The main impact of this treatment might be seen as a cleaning of the carbon-based particles of the material. Indeed, argon being inert, because of the temperature involved (1100 °C), the main result of the treatment is, as reported in the literature, the elimination of unstable oxygen-based functionalities [13]—oxygen being present in a significant amount in the precursors through the $\text{Fe}(\text{acac})_3$. Some nitrogen functionalities, such as amines or nitriles, and both oxygen–nitrogen functionalities, such as amides, are also eliminated at such a high temperature [14]. The thermal treatment under argon may also complete the washing with acetone performed on the pristine material, which is supposed to eliminate adsorbed species, such as polycyclic aromatic hydrocarbons. The treatment with ammonia resulted in a pronounced weight loss and provided a material with a very high specific surface area of $\approx 1130 \text{ m}^2\cdot\text{g}^{-1}$. This was one of the potential interests of NH_3 treatment, as a high specific surface area is likely to improve the ORR activity. It has been established, for a long time, that ammonia corrodes carbon at a high temperature, producing gaseous species such as HCN and H_2 , and therefore potentially producing porosity [15–18]. In the field of Fe/C/N ORR electrocatalysts, a strong correlation between the weight loss and the increase of the specific area has been established, which is mainly due to micropores formation [19]. For electrocatalysts prepared using carbon support, it has been shown that the efficiency of the ammonia corrosion, and therefore the high porosity formation, is related to the structural feature of the latter—the higher the amount of disordered carbon, the higher the efficiency of ammonia corrosion [20–22]. Finally, the high specific

surface area we obtained after the ammonia treatment on our pristine material is quite a noticeable and a very interesting result, as no particular component has been used in the precursor media with that goal, that is, particular carbon support—a sacrificial component. The efficiency of the ammonia treatment in promoting a high porosity might be due to a significant amount of disordered carbon existing in the pristine material, what has not been investigated here.

XRD was recorded for all of the samples (Figure 2) in order to get information on the iron phases formed during the different processes. The as-formed and argon annealed materials showed a wide contribution in the region centered at $2\Theta = 45^\circ$, in which numerous iron phases, such as carbide and nitride, can contribute [7]. The featureless pattern probably resulted from the small sized and poorly crystallized iron-based nanoparticles. The ammonia annealed material also showed a wide contribution overlapped by a diffraction pattern, tentatively attributed, at least partially, to $\text{Fe}_3\text{N}_{1.3}$. Other features could be observed—while too difficult to ascribe, they show that this latter nitride phase is not the only one present in the sample. In a previous report [7], the formation of iron nitride was suggested to be related to the successful formation of nitrogen-based ORR active sites in the carbon phase.

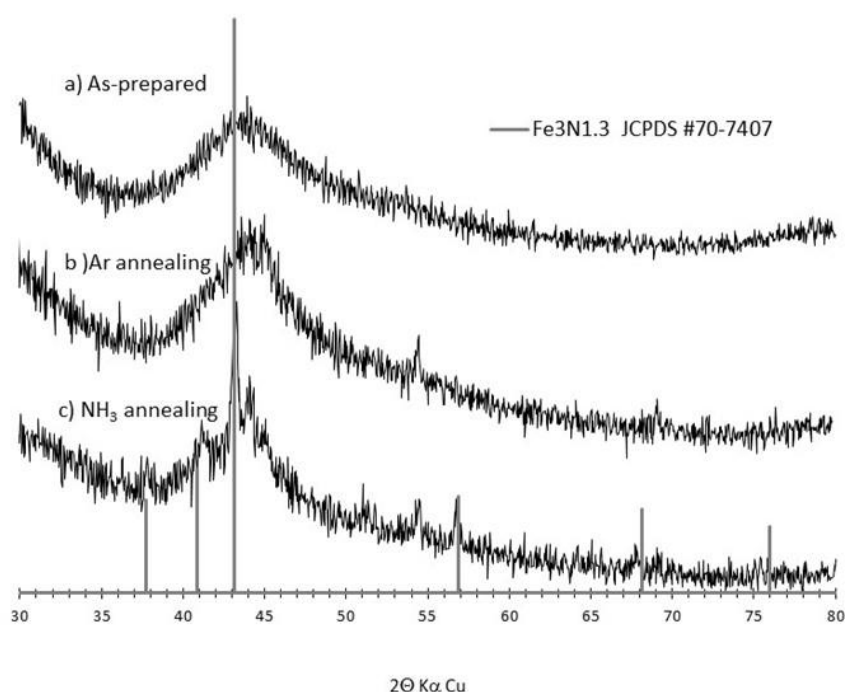


Figure 2. X-ray diffraction pattern recorded on as-formed, argon, and ammonia annealed materials.

The three materials were also characterized using transmission electron microscopy (Figure 3). The pristine material (Figure 3a) consists in chain-like agglomerated nanoparticles, whose diameter is about 20 nm. A careful observation of the micrograph reveals the presence of much smaller particles with a darker contrast, which could correspond to iron-based particles. Annealing (Figure 3b,c) keeps the size of the chain-like particles roughly unchanged, but a modification of the texture of the particles is observed for the material annealed under ammonia, which could be possibly related to the high specific surface area measured for this material.

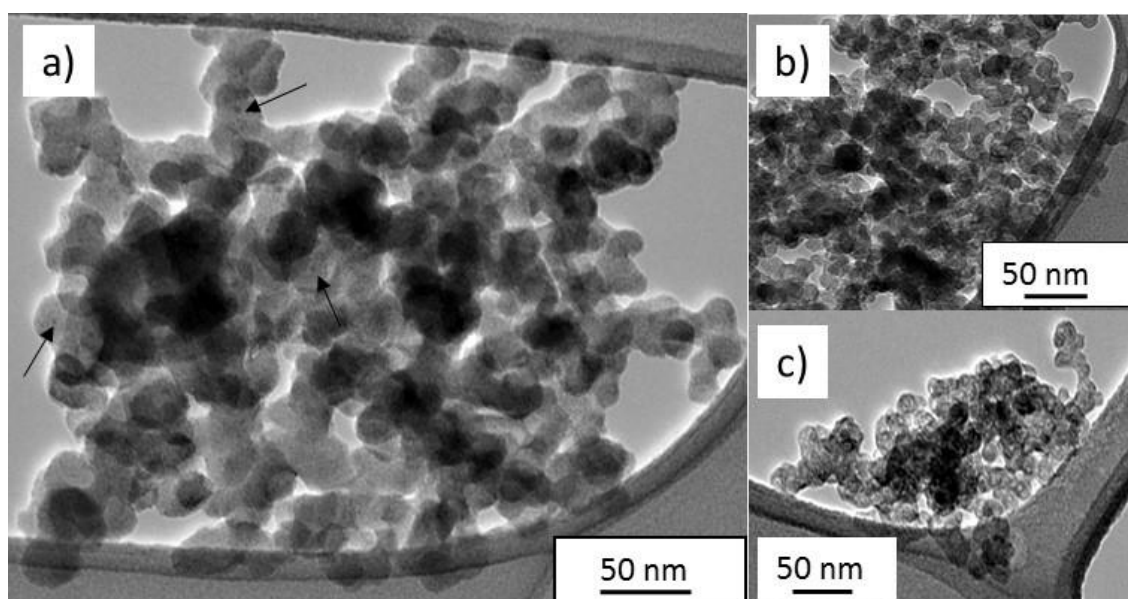


Figure 3. Transmission electron microscopy recorded on the as-formed (a), argon (b), and ammonia (c) thermally-treated materials.

The three different materials were finally analyzed by XPS, following the protocol described in the experimental section. Note that these data were collected after the electrodes had undergone an electrochemical conditioning step and an oxygen reduction measurement (see Experimental Section), as it led to a more representative composition of the material surface exposed to the electrolyte during ORR performance evaluation (next section). The XPS semi-quantitative analysis results are shown in Table 3 for the as-prepared and annealed materials.

Table 3. XPS semi-quantitative analysis recorded on as-formed materials, and annealed materials under argon and ammonia.

Material	C1s At.%	O1s At.%	N1s At.%	N1s/C1s At.%
As-prepared	92.0	4.6	3.4	0.037
Argon annealing	93.1	5.3	1.6	0.017
Ammonia annealing	96.2	2.3	1.5	0.016

The semi-quantitative analysis indicated that the surface of the material is essentially made of carbon. The as-formed material contained 3.4 At.% nitrogen, which here, is exclusively provided by the ammonia involved in the synthesis. When pyridine was used instead of toluene, it was found that the higher the R, the higher nitrogen content [7]; the latter being measured at 5.0 At.% for $R = 0.30$, that is, significantly higher than what is recorded here for toluene and $R = 0.40$. This could reflect a particular efficiency of pyridine, with respect to the incorporation of nitrogen into the nanomaterial. As in previous works, peak fitting was conducted, with an imposed peak full width at a half maximum of 1.5 eV [7]. Figure 4 shows that each spectrum can be fitted with four components, referred as N1, N2, N3, and N4, from low to high binding energies.

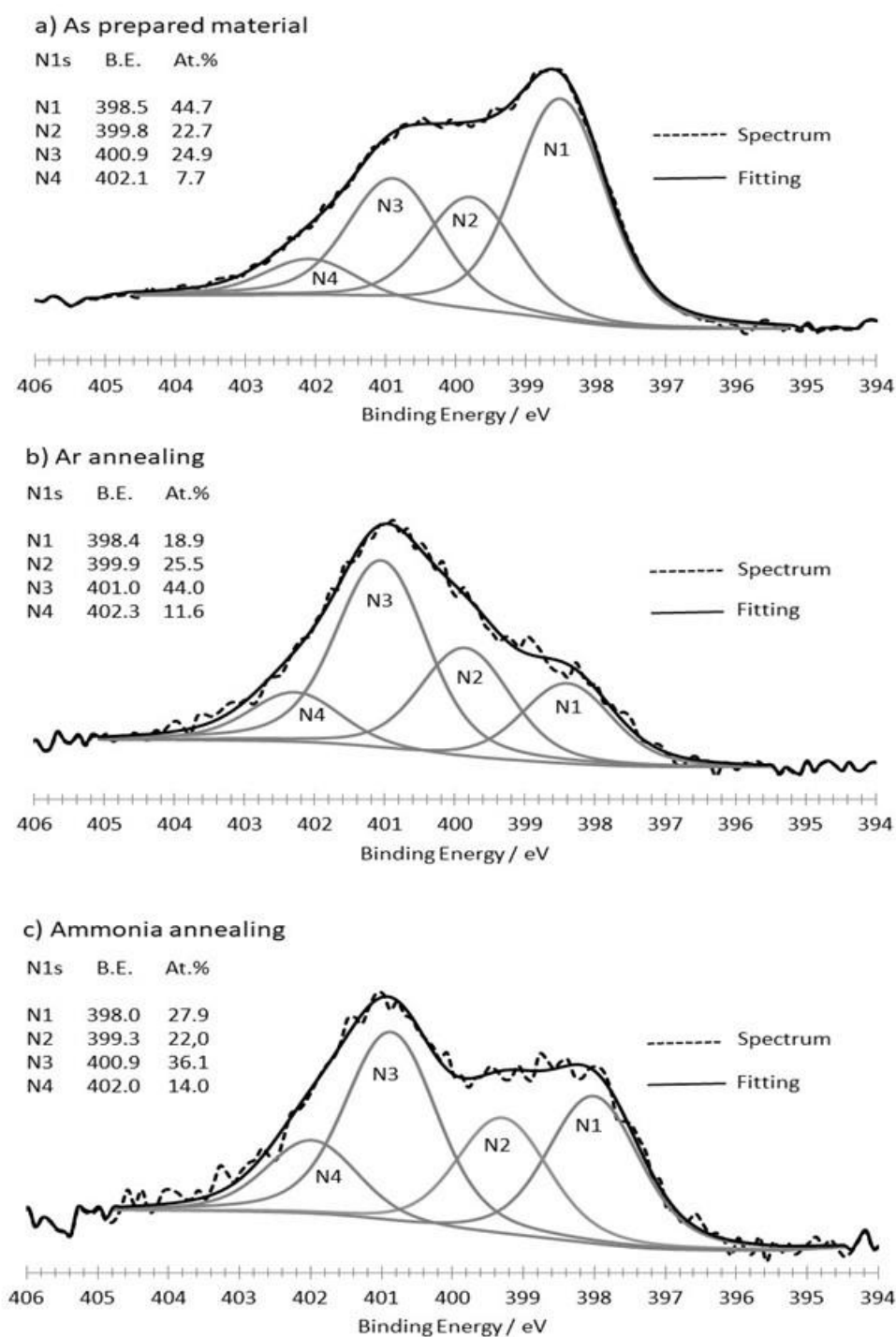


Figure 4. N1s XPS peak fitting of the as-formed and annealed materials. (a) As-formed material; (b) Argon annealed material; (c) Ammonia annealed material.

A major difference observed between the pristine material and the annealed ones is the drop in nitrogen content. The formation of the pristine material occurs in temperature conditions that are not known precisely, the region in which the precursors absorb the CO₂ laser variation is small and energy density is high, and a pyrolysis flame up to 10 cm in length forms, in which a gradient temperature exists. The nitrogen incorporation on the pristine material is due to ammonia, which is the only nitrogen precursor. Although we do not know whether NH₃ is completely dissociated or not, it is known that upon heating, it produces NH₂ and NH free radicals, which can react with carbon.

It seems reasonable to draw a parallel between our results and those recorded by XPS, when carbon is thermally treated with ammonia [17–23]. This literature reports that many different kinds of nitrogen functionalities can be formed in such conditions, among them, functionalities grafted at the edges of graphene planes, such as amine, imine, amide, and nitrile ones, which cover the wide N1s core level binding energy range [24]. These binding energies overlap with those recorded for the nitrogen species directly grafted in the graphene planes, such as of pyridine, pyrrole, and so-called graphitic N-sites. The latter nitrogen sites are among the nitrogen sites responsible for the ORR activity recorded in C/N/Fe. As will be seen in the next section, the pristine material exhibits a significant ORR activity, but much lower than that of the annealed materials. Therefore, one may assume that the XPS spectra of the as formed material shown in Figure 4a contains such active sites, but also a significant part of nitrogen functionalities grafted at the graphene plane edges, which are ORR inactive sites. This assumption also provides an explanation for the significant drop observed after the thermal treatment of the pristine material, as these ORR inactive nitrogenated sites are unstable at the temperature treatment used in this work (1100 °C).

We can now consider the differences observed between both spectra recorded for the annealed materials. The temperature treatment and duration being the same, the first assumption is that the nitrogen functionalities that are possibly eliminated compared to the pristine materials are identical in both thermally treated materials. It seems reasonable that, although the ammonia treatment of the pristine material can induce nitrogen functionalities formation such as those mentioned above in the case of a pristine material (amine, imine, etc.), these functionalities might be eliminated because of the high temperature involved. We assume here, that the N1 to N4 nitrogen species that are identified from the peak fitting shown in Figures 4b and 4c are the same in nature in both of the annealed materials. Indeed, the N1 to N4 binding energies for both of the annealed materials are, respectively, quite close to each other, and the differences observed (Figures 4b and 4c) lie in the range of those reported in the literature for those kinds of nitrogen sites on different nitrogen-doped carbon nanomaterials [24,25]. Based on the numerous literature related to nitrogen functionalities studied by N1s core level XPS analysis in carbon-based materials [23–27], N1 is attributed to N-Pyridinic, N2 to N-Pyrrole, and N3 and N4 to N-Graphitics, referred as center N-Graphitic and valley N-Graphitic, respectively. It is worth pointing that, as no iron is detected by the XPS analysis, the possible presence of FeN_x sites in the materials is not considered. Here, it looks to be of particular interest to consider the ratio of N_x functionalities for argon and ammonia treatments (Table 4), and to compare it to the unity.

Table 4. Ratios values for N_xNH₃/N_xAr species deduced from N1s spectra fitting of argon and ammonia treated materials.

	N1 _{NH3} /N1 _{Ar}	N2 _{NH3} /N2 _{Ar}	N3 _{NH3} /N3 _{Ar}	N4 _{NH3} /N4 _{Ar}
Ratio	1.47	0.86	0.82	1.21

The larger difference from N1 is observed for the N1 nitrogen (1.47); this strongly suggests that compared with the thermal treatment with argon, the ammonia treatment seems to favor the formation of pyridine-like nitrogen moieties. Note that the N_x ration for N4 sites (1.21) might be also significant. The major difference between the argon and ammonia treatment conditions is the chemical effect of ammonia. Ammonia is reported to induce the formation of pyridine-nitrogen (N1) from various kind oxygen functionalities [18,28]. Its ability to corrode carbon has been also closely related to the introduction of active sites towards the ORR, among them, graphite-like sites and pyridine-like ones. Furthermore, the need for ammonia to react with iron to form active sites towards the ORR [19], and the formation of iron nitride through ammonia treatment [29], as we can observe in Figure 2, are suspected to promote ORR active site formation. While the efficient role of ammonia treatment with respect to the formation of the N1 to N4 nitrogen sites appears obvious, the fact that the argon treatment results in the same surface nitrogen content as that for the NH₃ treatment is, at first glance, surprising. The treatment under argon most probably induces, at least partially, the transformation of nitrogen sites

incorporated in graphene planes as follows, pyrrole-like nitrogen converts to pyridine-like nitrogen, which converts to graphite-like nitrogen [26,30–32]. As the amount of pre-existing sites of these kinds of sites cannot be ascertained, it is not possible to know the extent to which the transformation of nitrogen sites incorporated in graphene planes occurs. Finally, the numerous events that can occur upon thermal treatments lead us to draw the conclusion that no definitive explanation can be given to the differences observed between the N1s spectra of argon and ammonia treated materials. However, it is worth pointing out that XPS probes the surface composition, and that although the carbon particle size, as shown by the TEM analysis (Figure 3), is the same, the specific surface areas for both materials are extremely different, which suggests a high porosity of the carbon-based particles treated under ammonia. For the latter, the extent to which the XPS analysis reflects the feature of the internal surface might be a pertinent question.

3.2. ORR Measurements

Figure 5 reports the ORR background corrected CVs recorded at $5 \text{ mV}\cdot\text{s}^{-1}$ for the three materials studied in this work.

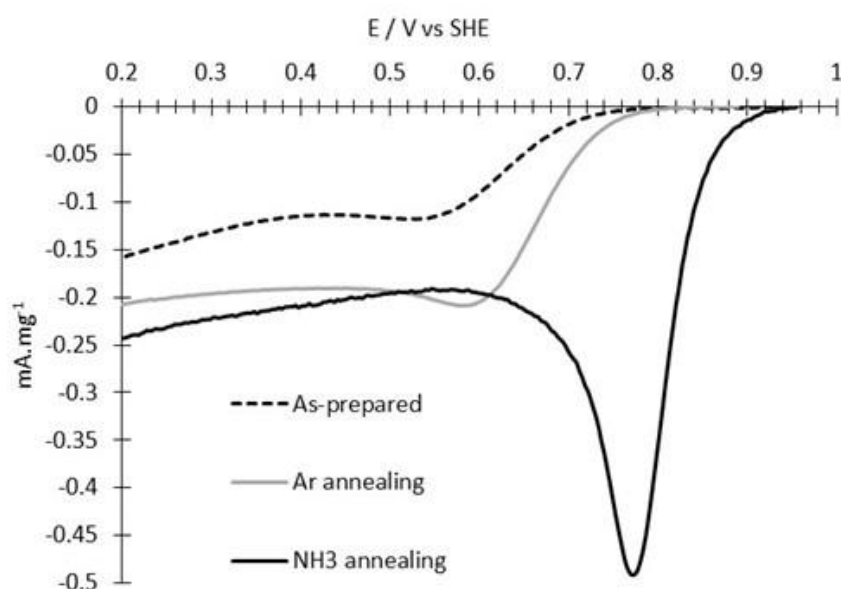


Figure 5. ORR background corrected CVs recorded at $5 \text{ mV}\cdot\text{s}^{-1}$ in HClO_4 1M for the as-formed, and argon and ammonia thermally treated materials, based porous electrodes. The electrode loadings are 3.82, 3.24, and $2.29 \text{ mg}\cdot\text{cm}^{-2}$, respectively, and the geometrical electrode area is 0.785 cm^2 .

The as-formed material showed an onset ORR potential at $\approx 790 \text{ mV}$. The trend observed for the materials prepared from pyridine as a function of R, is that the higher the R, the higher the onset potential. For $R = 0.30$, the onset potential was found to be $\approx 860 \text{ mV}$ (i.e., $\approx 90 \text{ mV}$ higher than the material obtained here with toluene at $R = 0.40$). This suggests, again, a particular efficiency of pyridine, not only in the incorporation of nitrogen in the material, but also in the formation of active sites for the ORR.

Compared to the pristine material, annealing resulted in an improvement of the ORR response for both atmosphere conditions. Treatment under argon improved the ORR onset potential by about 30 mV . Such an improvement might be related to the cleaning of the particle surface, as well as of the nitrogen sites transformation evocated above. With the treatment temperature being high, an improvement of the conductivity of the material may also impact the ORR response. The modification of the latter observed after ammonia treatment is much stronger, by about 120 mV , compared to the as-formed material. This might be reasonably attributed to the very high specific surface area of this catalyst, which probably results in a strong volume density of ORR active sites in the catalyst layer. Figure 5

provides typical ORR CVs at $5 \text{ mV}\cdot\text{s}^{-1}$, which were recorded after the conditioning step involving a prolonged cycling at $100 \text{ mV}\cdot\text{s}^{-1}$ under O_2 (see Experimental Section 2.5). It is worth noting that several electrodes with different loadings were prepared for both of the annealed materials, giving identical ORR responses for each material, respectively (Appendix A, Figure A1a,b). Other samples were successively scanned at higher scan speeds (Appendix A, Figure A1c,d), and showed expected ORR responses with increasing peak currents, and a peak potential shifted at lower potentials [10,11]. These additional data confirmed that the CVs shown in Figure 5 reflect the ORR performances of the annealed materials.

The difference in the ORR performances between both of the annealed materials is also revealed by the selectivity measurement performed on the porous electrodes [12]. The latter is based on H_2O_2 assaying in the electrolyte, in which porous electrodes with different loadings are submitted to the ORR at a given potential during the chronoamperometry experiment (see Section 2.5). The potential chosen for this measurement is the one obtained for the ORR peak current recorded at $5 \text{ mV}\cdot\text{s}^{-1}$ in HClO_4 0.1 M. Appendix B provides an example of the ORR chronoamperometry experiment recorded under stirring for 30 min for one electrode sample of each thermally treated material. It is worth pointing to the stability of the ORR current, and thus the stability of the catalyst's performance over the time measurement. Figure 6 reports the selectivity and the potential at which it has been measured for both materials. The material annealed under argon shows a critical loading of about $3 \text{ mg}\cdot\text{cm}^{-2}$, from which the selectivity becomes constant with an average of ≈ 3.6 electrons exchanged. The material annealed under ammonia, which shows a much higher ORR activity, a critical loading lower than $0.3 \text{ mg}\cdot\text{cm}^{-2}$, and a much higher selectivity of ≈ 3.9 electrons.

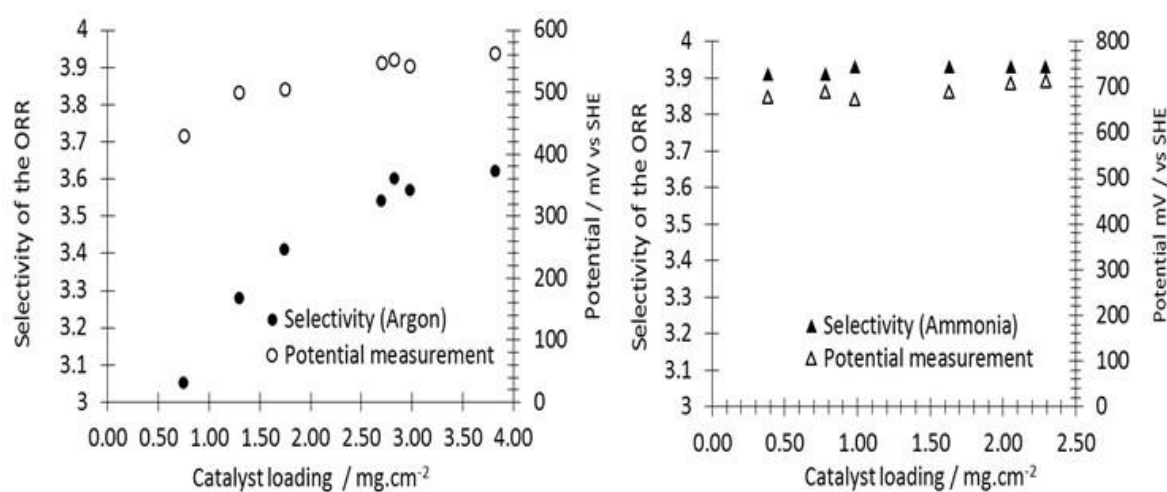


Figure 6. Trends recorded for the selectivity for the materials annealed under argon and annealed under ammonia, and the potential at which the selectivity of the ORR has been measured.

4. Conclusions

In this work, we investigated the effect of the high-temperature annealing of one Fe/C/N ORR electrocatalyst prepared by laser pyrolysis from a simple nebulized liquid precursor media based on toluene and iron acetylacetonate. It was shown that such a treatment conducted under ammonia results in the formation of a catalyst with a very high specific surface area and a high ORR activity and selectivity. This result markedly contrasts with the reports from the literature about the synthesis of Fe/C/N with a very high specific surface area, which generally requires multistep procedures and thermal treatments, and/or the use of dedicated sacrificial or templating components among the precursors. CO_2 laser pyrolysis is therefore a process that can produce Fe/C/N electrocatalysts with a very high ORR activity and good selectivity in acid media, starting from a very simple liquid precursor media, and using a single thermal post-treatment under ammonia.

Author Contributions: H.P. proposed and guided this research, and wrote the paper. V.J. recorded the XRD experiments and performed the data analysis with H.P. J.V., M.F., and A.E. carried out the XPS experiments and aided in the interpretation and data treatment with H.P. A.Q., O.S., Y.L., H.P., and V.J. were involved in the laser pyrolysis syntheses. H.P. and V.J. processed the as-prepared materials, prepared porous electrode elaboration, and performed electrochemical measurements. V.J. recorded the X-ray fluorescence measurements and BET measurements.

Funding: The Region Ile-de-France in the framework of DIM Nano-K supported this work.

Acknowledgments: Y. Rousseau is warmly acknowledged for the recording of the T.E.M. images.

Conflicts of Interest: The authors declare no conflict of interest.

Appendix A

Supporting information section related to the ORR electrochemical measurements on NH_3 and the Argon annealed materials.

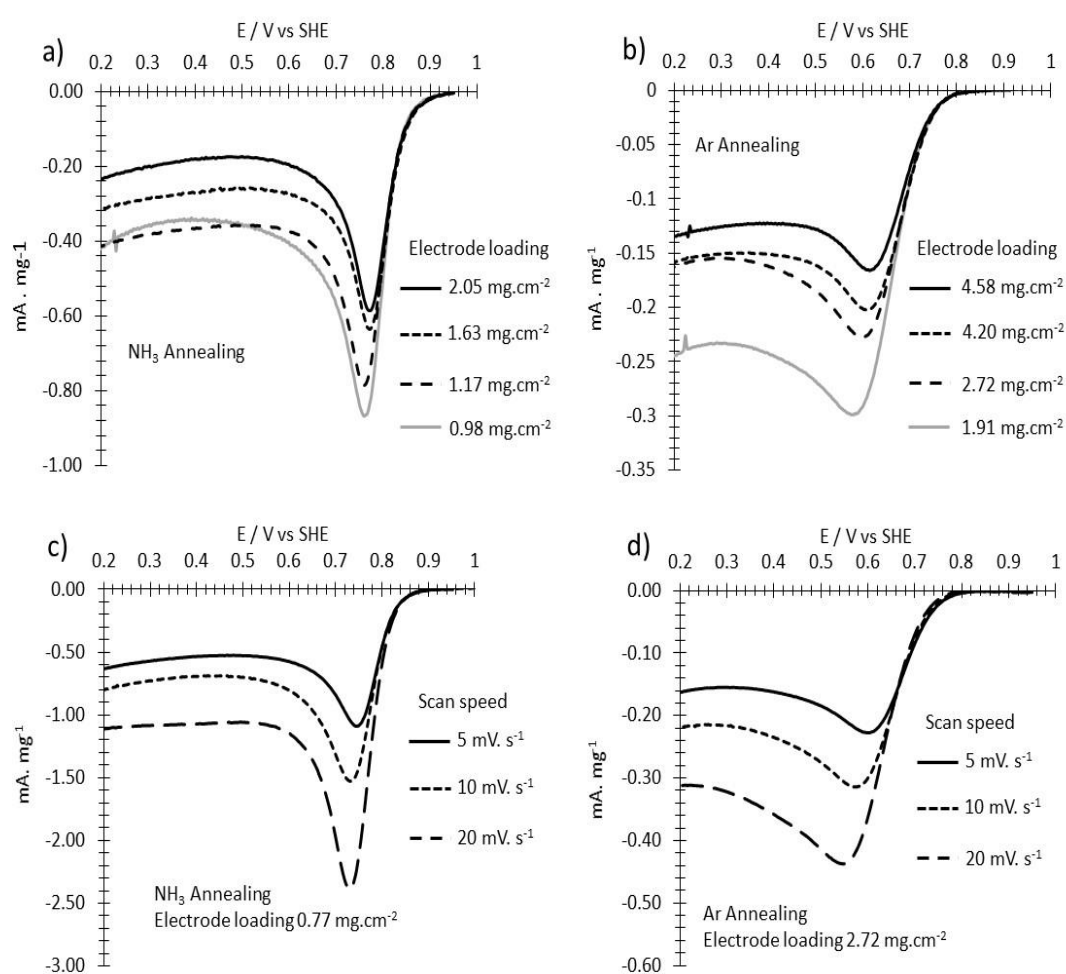


Figure A1. (a) Background corrected ORR CVs recorded at $5 \text{ mV}\cdot\text{s}^{-1}$ for several electrodes with different catalyst loadings, prepared from the material annealed under NH_3 . (b) Background corrected ORR CVs recorded at $5 \text{ mV}\cdot\text{s}^{-1}$ for several electrodes with different catalyst loadings, prepared from the material annealed under Ar. (c) Background corrected ORR CVs recorded on the same electrode at three different scan speeds ($5 \text{ mV}\cdot\text{s}^{-1}$, $10 \text{ mV}\cdot\text{s}^{-1}$, and $20 \text{ mV}\cdot\text{s}^{-1}$) for the material annealed under NH_3 . (d) Background corrected ORR CVs recorded on the same electrode at three different scan speeds ($5 \text{ mV}\cdot\text{s}^{-1}$, $10 \text{ mV}\cdot\text{s}^{-1}$, and $20 \text{ mV}\cdot\text{s}^{-1}$) for the material annealed under Ar.

Appendix B

Supporting information related to selectivity measurement, which illustrates the stability of the ORR response over the experiment duration.

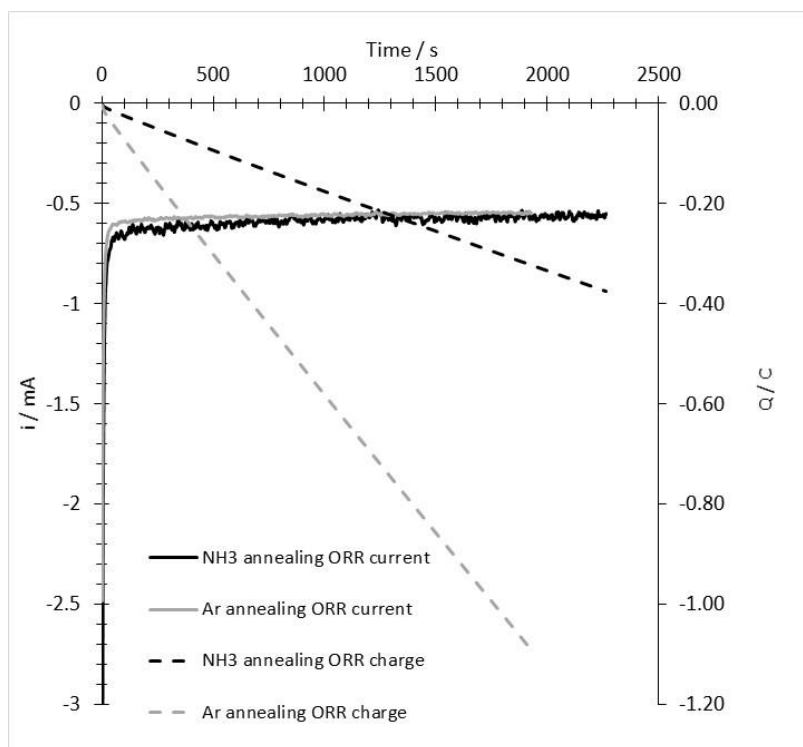


Figure A2. Examples of ORR chronoamperometry measurements (and corresponding charge) performed on an NH_3 annealed electrode sample (black lines) and an Ar annealed electrode sample (grey lines). The loading for the NH_3 annealed electrodes sample is $2.29 \text{ mg}\cdot\text{cm}^{-2}$, and the loading for the Ar annealed electrode sample is $3.82 \text{ mg}\cdot\text{cm}^{-2}$. The selectivities calculated for both of the electrodes are shown in Figure 6.

References

1. Shao, M.; Chang, Q.; Dodelet, J.-P.; Chenitz, R. Recent advances in electrocatalysts for oxygen reduction. *Chem. Rev.* **2016**, *116*, 3594–3657. [[CrossRef](#)] [[PubMed](#)]
2. Chokai, M.; Daidou, T.; Nabae, Y. Development of Pt-Free Carbon-Based Catalyst for PEFC Cathode Prepared from Polyacrylonitrile. *ECS Trans.* **2014**, *64*, 261–270. [[CrossRef](#)]
3. Proietti, E.; Jaouen, F.; Lefevre, M.; Larouche, N.; Tian, J.; Herranz, J.; Dodelet, J.-P. Iron-based cathode catalyst with enhanced power density in polymer electrolyte membrane fuel cells. *Nat. Commun.* **2011**, *2*, 416. [[CrossRef](#)]
4. Shuia, J.; Chena, C.; Grabstanowicza, L.D.; Zhao, D.; Di-Jia Liua, D.-J. Highly efficient nonprecious metal catalyst prepared with metal–organic framework in a continuous carbon nanofibrous network. *2015-PNAS* **2015**, *112*, 10631–10634. [[CrossRef](#)] [[PubMed](#)]
5. Serov, A.; Artyushkova, K.; Atanassov, P. Fe-N-C Oxygen Reduction Fuel Cell Catalyst Derived from Carbendazim: Synthesis, Structure, and Reactivity. *Adv. Energy Mater.* **2014**, *4*, 1301735. [[CrossRef](#)]
6. Ratso, S.; Sahraie, N.R.; Sougrati, M.T.; Käärik, M.; Kook, M.; Saar, R.; Paiste, P.; Jia, Q.; Leis, J.; Mukerjee, S.; et al. Synthesis of highly-active Fe–N–C catalysts for PEMFC with carbide-derived carbons. *Mat. Chem.* **2018**, *6*, 14663–14674. [[CrossRef](#)]
7. Perez, H.; Jorda, V.; Bonville, P.; Vigneron, J.; Frégnaux, M.; Etcheberry, A.; Quinsac, A.; Habert, A.; Leconte, Y. Synthesis and characterization of Carbon/Nitrogen/Iron based nanoparticles by laser pyrolysis as non-noble metal electrocatalysts for oxygen reduction. *C* **2018**, *4*, 43. [[CrossRef](#)]

8. Jahnke, H.; Schönborn, M.; Zimmermann, G. Organic dyestuffs as catalysts for fuel cells. *Top. Curr. Chem.* **1976**, *61*, 133–181. [[CrossRef](#)] [[PubMed](#)]
9. Osmieri, L. Transition Metal-Nitrogen-Carbon (M-N-C) catalysts for oxygen reduction reaction. Insights on synthesis and performance in polymer electrolyte fuel cells. *Chem. Eng.* **2019**, *3*, 16. [[CrossRef](#)]
10. Cheng, X.; Than, X.-T.; Pinault, M.; Mayne, M.; Reynaud, C.; Vigneron, J.; Etcheberry, A.; Perez, H. Determination of selectivity and specific area related to oxygen reduction reaction as a function of catalyst loading on non-noble metal based electrocatalyst porous electrodes: An example on nitrogen doped carbon nanotube. *Electrochim. Acta* **2014**, *135*, 293–300. [[CrossRef](#)]
11. Cheng, X.; Volatron, F.; Pardieu, E.; Borta, A.; Carrot, G.; Reynaud, C.; Mayne, M.; Pinault, M.; Etcheberry, A.; Perez, H. Nanocomposite electrodes based on pre-synthesized organically grafted platinum nanoparticles and carbon nanotubes III. Determination of oxygen reduction reaction selectivity and specific area of porous electrode related to the oxygen reduction reaction ranging from $2 \text{ m}^2.\text{gPt}^{-1}$ to $310 \text{ m}^2.\text{gPt}^{-1}$. *Electrochim. Acta* **2013**, *89*, 1–12. [[CrossRef](#)]
12. Cheng, X.; Challier, L.; Etcheberry, A.; Noël, V.; Perez, H. The ABTS-HRP system as an alternative method to RRDE for the determination of the selectivity of the oxygen reduction reaction. *Int. J. Electrochem. Sci.* **2012**, *7*, 6247–6264.
13. De la Puente, G.; Pis, J.J.; Menhdez, J.A.; Grange, P. Thermal stability of oxygenated carbons functions in activated carbons. *J. Anal. Appl. Pyrolysis* **1997**, *43*, 125–138. [[CrossRef](#)]
14. Jansen, R.J.J.; Van Bekkum, H. XPS of nitrogen-containing functional groups on activated carbons. *Carbon* **1995**, *33*, 1021–1027. [[CrossRef](#)]
15. Boehm, H.P. Some aspects of the surface chemistry of carbon blacks and other carbons. *Carbon* **1994**, *32*, 759–769. [[CrossRef](#)]
16. Sherwood, T.K.; Gilliland, E.R.; Ing, S.W. Hydrogen Cyanide Synthesis from Elements and from Ammonia and Carbon. *Ind. Eng. Chem.* **1960**, *52*, 601–604. [[CrossRef](#)]
17. Abotsi, G.M.K.; Scaroni, A.W. Reaction of carbons with ammonia: Effects on the surface charge and molybdenum adsorption. *Carbon* **1990**, *28*, 79–84. [[CrossRef](#)]
18. Stöhr, B.; Boehm, H.P.; Schlögl, R. Enhancement of the catalytic activity of activated carbons in oxydation reactions by thermal treatment with ammonia or hydrogen cyanide and observation of a superoxide species as a possible intermediate. *Carbon* **1991**, *29*, 707–720. [[CrossRef](#)]
19. Jaouen, F.; Lefèvre, M.; Dodelet, J.-P.; Cai, M. Heat-Treated Fe/N/C Catalysts for O₂ Electroreduction: Are Active Sites Hosted in Micropores? *J. Phys. Chem. B* **2006**, *110*, 5553–5558. [[CrossRef](#)] [[PubMed](#)]
20. Jaouen, F.; Charretier, F.; Dodelet, J.-P. Fe-Based Catalysts for Oxygen Reduction in PEMFCs Importance of the Disordered Phase of the Carbon Support. *J. Electrochem. Soc.* **2006**, *153*, A689–A698. [[CrossRef](#)]
21. Charretier, F.; Jaouen, F.; Ruggeri, S.; Dodelet, J.-P. Fe/N/C non-precious catalysts for PEM fuel cells: Influence of the structural parameters of pristine commercial carbon blacks on their activity for oxygen reduction. *Electrochim. Acta* **2008**, *53*, 2925–2938. [[CrossRef](#)]
22. Jaouen, F.; Dodelet, J.-P. Non-Noble Electrocatalysts for O₂ Reduction: How Does Heat Treatment Affect Their Activity and Structure? Part, I. Model for Carbon Black Gasification by NH₃: Parametric Calibration and Electrochemical Validation. *J. Phys. Chem. C* **2007**, *111*, 5963–5970. [[CrossRef](#)]
23. Shafeeyan, M.S.; Wan Daud, W.M.A.; Houshmand, A.; Sharimi, A. A review on surface modification of activated carbon for carbon dioxide adsorption. *J. Anal. Appl. Pyrolysis* **2010**, *89*, 143–151. [[CrossRef](#)]
24. Jimenez-Mateos, J.M.; Fiero, J.L.G. X-ray Photoelectron Spectroscopic Study of Petroleum Fuel Cokes. *Surf. Interface Anal.* **1996**, *24*, 223–226. [[CrossRef](#)]
25. Susi, T.; Pichler, T.; Ayala, P. X-Ray photoelectron spectroscopy of graphitic carbon nanomaterials doped with heteroatoms. *Beilstein J. Nanotechnol.* **2015**, *6*, 177–191. [[CrossRef](#)]
26. Pels, J.R.; Kapteijn, F.; Moulijn, J.A.; Zhu, Q.; Thomas, K.M. Evolution of nitrogen functionalities in carbonaceous materials during pyrolysis. *Carbon* **1995**, *33*, 1641–1653. [[CrossRef](#)]
27. Casanovas, J.; Ricart, J.M.; Rubio, J.; Illas, F.; Jimenez-Mateos, J.M. Origin of the Large N 1s Binding Energy in X-ray Photoelectron Spectra of Calcined Carbonaceous Materials. *J. Am. Chem. Soc.* **1996**, *118*, 8071–8076. [[CrossRef](#)]
28. Jansen, R.J.J.; Van Bekkum, H. Amination and ammoxidation of activated carbons. XPS of nitrogen-containing functional groups on activated carbons. *Carbon* **1994**, *32*, 1507–1516. [[CrossRef](#)]

29. Kramm, U.I.; Herrman-Geppert, I.; Bogdanoff, P.; Fiechter, S. Effect of an ammonia treatment on structure, composition, and oxygen reduction reaction activity of Fe-N-C catalysts. *J. Phys. Chem. C* **2011**, *115*, 23417. [[CrossRef](#)]
30. Sharifi, T.; Hu, G.; Jia, X.; Wagberg, T. Formation of Active Sites for Oxygen Reduction Reactions by Transformation of Nitrogen Functionalities in Nitrogen-Doped Carbon Nanotubes. *ACS Nano* **2012**, *6*, 8904–8912. [[CrossRef](#)] [[PubMed](#)]
31. Stanczyk, K.; Dziembaj, R.; Piwowarska, Z.; Witkowski, S. Transformation of nitrogen structures in carbonization of model compounds determined by XPS. *Carbon* **1995**, *33*, 1383–1392. [[CrossRef](#)]
32. Arrigo, R.; Hävecker, M.; Schlögl, R.; Su, D.S. Dynamic surface rearrangement and thermal stability of nitrogen functional groups on carbon nanotubes. *Chem. Commun.* **2008**, *40*, 4891–4893. [[CrossRef](#)] [[PubMed](#)]



© 2019 by the authors. Licensee MDPI, Basel, Switzerland. This article is an open access article distributed under the terms and conditions of the Creative Commons Attribution (CC BY) license (<http://creativecommons.org/licenses/by/4.0/>).